Experimental Investigation of a Strongly Shocked Gas Bubble

Devesh Ranjan, Mark Anderson, Jason Oakley, and Riccardo Bonazza*

Engineering Physics Department, University of Wisconsin-Madison, 1500 Engineering Dr., Madison, Wisconsin 53706, USA

(Received 10 November 2004; published 12 May 2005)

A free-falling, spherical, soap-film bubble filled with argon is subjected to a planar $M = 2.88$ shock in atmospheric nitrogen; vorticity is deposited on the surface of the bubble during shock interaction, and the Richtmyer-Meshkov instability ensues. The geometrical development of the shocked bubble is diagnosed with laser sheet imaging and a planar slice showing two cross sections of both the major vortex ring and a secondary vortex ring is revealed experimentally for the first time. Quantitative measurements of the experimental data include the vortex velocity defect, and subsequent circulation calculations, along with a new set of relevant length scales. The shock wave strength, leading to a post-shock compressible regime, allows the study of the instability development in a regime between low Mach number shock tube experiments and high Mach number laser driven experiments that has not been investigated previously.

DOI: 10.1103/PhysRevLett.94.184507 PACS numbers: 47.40.Nm, 47.20.Bp, 47.20.Ma

The Richtmyer-Meshkov (RM) instability [1,2] occurs at an interface between two fluids when the passage of a shock wave results in the baroclinic deposition of vorticity ($\nabla\rho \times \nabla p \neq 0$) on the interface. In the special case of a spherical bubble and planar shock wave, the RM instability deforms the bubble into a torus-shaped vortex ring. The first experimental observation of the transformation of a spherical bubble into a vortex ring was for a shock wave accelerating an expanding burning gas [3]. This experimental technique has the advantage of a gas-gas interface between the bubble and the surrounding fluid; however, there are unknown thermodynamic gradients within the bubble. Haas and Sturtevant [4] conducted experiments on soap bubbles 5 cm in diameter (filled with He and R22), supported by a holder in a horizontal shock tube, subjected to a $M < 1.3$ shock in air. The presence of a vortex ring structure was suggested by the images and inferred from the velocity measurements; however, due to the integral visualization technique employed, the structure of the vortex was not visualized. These experiments were later modeled numerically in two dimensions [5,6] with the results being in “close” agreement to the experiment. Analogous to the shocked spherical bubble experiments, cylindrical inhomogeneities have also been studied experimentally [4,7] with similar observed vortex ring characteristics; numerical simulations show “excellent” agreement [8] with weak-shock ($M < 1.3$) experiments. Very high Mach number ($M > 10$) experiments, using a laser driven polystyrene shock tube [9,10], have been used to accelerate a copper sphere to study the RM instability. The results of the high Mach number experiments showed strong three-dimensional effects, diagnosed with face-on radiography, due to the azimuthal bending-mode instability (Widnall-type instability).

When the particle velocity behind a shock wave becomes supersonic ($M = 2.07$ in atmospheric nitrogen), a transition may occur where compressibility effects (negligible for weak shocks) alter the ensuing bubble growth. New experiments at the Wisconsin Shock Tube Laboratory [11,12] study a shocked bubble ($M = 2.88$) in an effort to gain understanding in a regime above the previous low M shock tube experiments where compressibility effects are beginning to impact the flow and below the shock strengths achieved in laser driven experiments. A vertical shock tube with a height of 9.2 m and a 25.4 cm square cross section is used; Fig. 1 shows a schematic overview of the experimental system used here to study the interaction of a planar shock wave with a spherical density inhomogeneity. A soap bubble is created with a stainless steel injection system by first displacing any nitrogen in the injector with Ar, then placing a layer of soap film on the tip of the bubble injector, and finally, using a pneumatic cylinder of prescribed volume to blow an argon bubble, approximately 5 cm in diameter. This process ensures purity of argon inside the bubble while minimizing the argon contamination of the surrounding nitrogen to less than 1%. The soap film is estimated to be 0.5 μm thick [13,14] with a slight

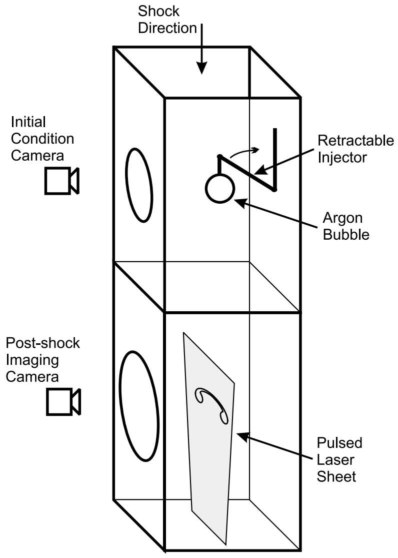

FIG. 1. Experimental setup.

increase in thickness at the bottom of the bubble due to gravitational flow of the soap film. In a predetermined amount of time, anywhere from 50–100 ms before shock interaction with the bubble, the bubble is released from the injector by a fast retraction of the injector into a slot located in the shock tube wall. This results in a clean experiment where the argon bubble is in free fall in a nitrogen atmosphere and the disruption to the planar shock (that would occur if a holder was left in the flow cross section) is minimized. After release, the bubble oscillates on a time scale of 100 ms remaining nearly spherical with an eccentricity of 0.26 ± 0.03. The release and free fall of the bubble are recorded at 250 fps with a CCD camera (DALSA CA-D1-0256A) and front lighting. This allows the capture of the evolution of the bubble during its release from the holder and provides an initial condition image of the bubble prior to (within 10 ms) shock interaction, during which the vorticity is deposited and the RM instability initiates.

The interaction and mixing of the shock wave with the bubble is imaged with a planar laser sheet produced from a *Q*-switched Nd:YAG laser (Continuum Surelite II). The laser beam is formed into a plane and transmitted through the center of the bottom of the shock tube. The laser is capable of two pulses separated by a minimum of 100 ns with a pulse width of 10 ns duration. A 1024×1024 pixel array Andor (model 434) CCD camera is used to capture the Mie scattered light resulting from the laser interaction with the soap-film solution (the soap film is atomized during interaction with the strong shock). The two laser pulses allow the capture of two shocked bubble images on a single frame of the CCD array enhancing the investigation of the evolution of the instability during a single experiment. Several experiments have been conducted and the reproducibility between different experiments is quite good with bubble diameters in the range $D = 5.0 \pm 0.02$ cm and incident Mach numbers in the range 2.88 ± 0.04.

Figure 2 shows the evolution of the shocked spherical density inhomogeneity after contact with a $M = 2.88$ shock with a wave velocity of 1017 m/s and an N_2 particle velocity $u_p = 745$ m/s. The time is nondimensionalized as $\tau = t/\tau'$, where τ' is defined as the cloud crushing time, $\tau' = D/u_p$. The initial condition [Fig. 2(a)] shows the bubble being held by the injector prior to the injector retracting and the arrival of the shock. The bubble is seen to be slightly elliptical due to the density difference between the nitrogen atmosphere and the argon gas within the bubble, and the presence of a small accumulation of the soap fluid on the bottom portion of the bubble due to gravitational forces on the soap film. The initial stages of shock interaction result in the compression of the bubble as shown in Fig. 2(b). The top bright portion of the image shows the shocked part of the bubble with the lower horizontal surface as the shock front. At this stage the unshocked region of the bubble is still intact and, although faint, can still be seen. During this period of shock interaction, vorticity is deposited due to the misalignment of the density and pressure gradients which later result in the formation of several vortex rings. Figure 2(c) shows the bubble when the shock is approximately 1.5 diameters downstream and the bubble has been compressed into an inverted bowl-type shape. At this point the soap film has been atomized and the average droplet size is estimated to be on the order of 1 μm [15,16]. The fluid on the outer edges of the bubble is beginning to swirl due to the strong vortex ring generated during initial shock interaction. The next phase of the evolution begins in Fig. 2(d) when the upper surface of the bubble is becoming distorted and a secondary vortex ring associated with the appearance of an upper mushroom structure is becoming evident. The bubble asymmetry about the vertical axis is due to the onset of a Widnall-type instability. The next image in time [Fig. 2(e)] has three notable features: the major vortex ring on the bottom of the image entrains fluid from the center portion of the shocked bubble and swirls it into the center of the vortex ring. The major vortex ring is connected at the top of the image through a cone-shaped channel (appears as the bright lines in the two dimensional image) forming an approximately 45 ° angle to the horizontal. This channel continues to shrink in thickness and

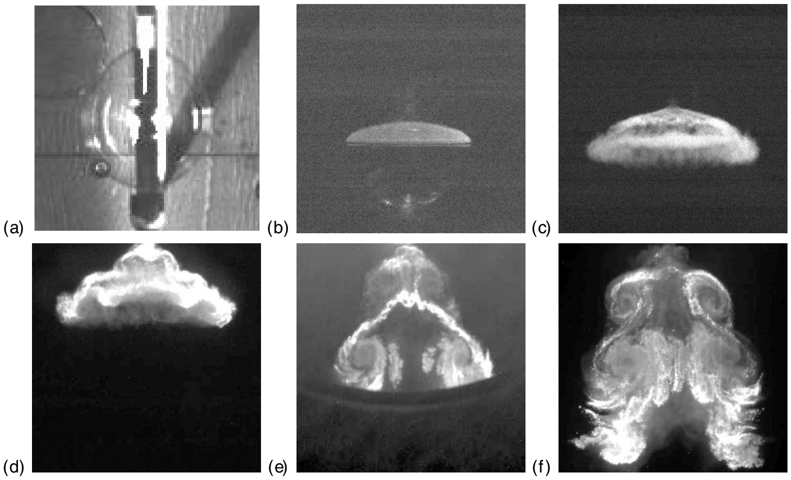

FIG. 2. Experimental images of a shocked ($M = 2.88$) argon bubble in N_2: (a) initial condition, (b) $\tau = 0.35$, (c) $\tau = 2.49$, (d) $\tau = 4.09$, (e) $\tau = 7.99$, and (f) $\tau = 10.82$.

increases in length as the fluid is pulled into the vortex. The third major feature is the growth of the smaller minor vortex ring on top of the bubble which is similar to that calculated numerically for a R12 bubble [17] but never confirmed experimentally. Figure 2(f) is at a much later time, when the shock is approximately ten bubble diameters downstream. At this point in the evolution, the bubble appears to be undergoing a lot of fine-scale turbulent mixing in addition to major length scale growth. The major vortex ring has pulled the fluid from above into the central portion previously filled with nitrogen gas and also tails of fluid appear to develop from the bottom vortex. The upper vortex seems to be progressing in a similar manner to the bottom but at longer time scales.

Figure 3 shows the vortex velocity V_v, nondimensionalized by the shocked gas particle speed as a function of time. At early times, the velocity is that of the bubble whose location is measured as the average of the top and bottom of the bubble. At later times, the vortex velocity is measured for experiments where two shocked bubble images are obtained on a single image; the measurement error is on the order of 1% based on the spatial accuracy of the CCD image and the timing jitter for the two laser pulses. The velocity defect behaves in a similar fashion to a weakly shocked krypton bubble in air [18], that is, the bubble initially accelerates to the particle velocity (within the experimental error), and then the vortex velocity falls back below the particle velocity at later times. The vorticity deposited on the surface of the bubble results in a residual circulation in the major vortex ring at late times which can be calculated from the velocity defect [4]; this circulation is calculated to be -3.7 and -4.8 m^2/s at the respective times $\tau = 8.0$ and 8.7. The negative sign results from a velocity defect less than unity and the magnitude is much higher than previously measured in weak-shock experiments [4]. This late time circulation calculation can be contrasted to an estimation of the initial circulation which is -8.6 m^2/s; this is calculated according to the same formula used for a weakly shocked, spherical, Freon-22 bubble [5].

Figure 4 shows five relevant length scales of the shocked bubble that have not been correlated previously: w is the maximum width, $h1$ is the overall height, $h2$ is the height from the bottom of the vortex to the apex of the cone-shaped channel, vd is the maximum vortex diameter, and vs is the vortex spacing from core to core. The dashed line A–A indicates the location of a pixel lineout shown beneath the image and it is from such a lineout that the lengths are measured. For example, vs is determined by stretching the lineout at location A–A, and measuring the distance between the points where local minima are identified in the visual center of the vortex. In the analysis, the length scales are nondimensionalized by the initial bubble diameter (D), e.g., $L_w = w/D$.

Figure 5 shows the width, height, and vortex size measurements, and three regions of interest are observed, separated with the dashed vertical lines on the plots: region 1 is the compression zone ($0 < \tau < 2.8$); region 2 is the vortex-pair-induced mixing zone ($2.8 < \tau < 6.9$); and region 3 is the highly turbulent mixing zone ($\tau > 7$). The earliest post-shock picture shows an initial flattening of the bubble caused by the compression of the shock wave. From the height plot [Fig. 5(b)] the compression is observed taking place until $\tau = 2.8$, after which, both L_{h1} and L_{h2} start to grow. This flattening is observed in the width plot [Fig. 5(a)] where L_w has reached a local maximum. Near $\tau = 4$ the width suddenly decreases due to the shock wave reflected from the shock tube side walls which originated when the incident shock wave refracted off the surface of the bubble. The influence of the shock tube walls on w was discussed previously in a numerical study of a weakly shocked bubble [19]. The compression observed in the images [Figs. 2(b) and 2(c)] shows there is negligible visible mixing of the gases in this region. The vortex formation begins at $\tau = 3.4$ [Fig. 5(c)] in region 2 where the height is increasing rapidly and the width, which has reached a plateau, decreases. The formation of the vortex ring enhances the mixing and this is evident in the rapid increase in the vortex diameter. The vortex spacing decreases during this time and reaches a minimum at $\tau = 6.9$, which is explained by the vortex diameter increasing (while the w growth has been retarded by the reflected

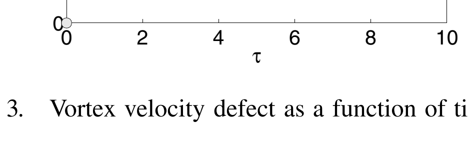

FIG. 3. Vortex velocity defect as a function of time.

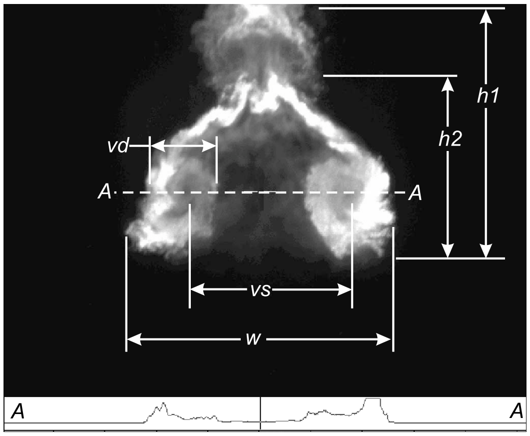

FIG. 4. Bubble length scales.

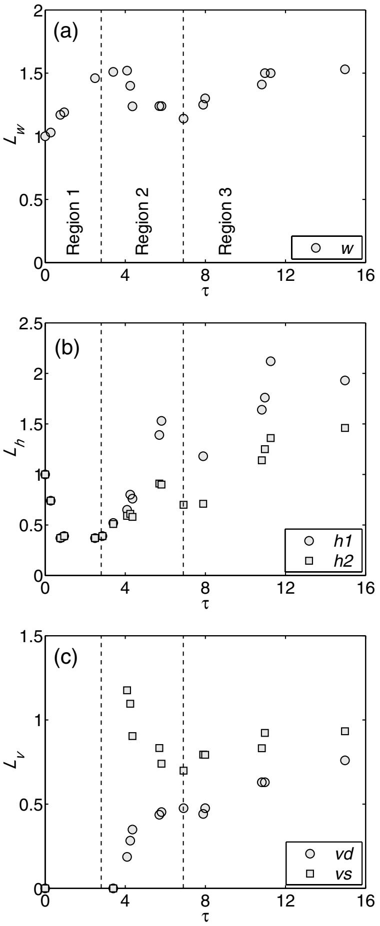

FIG. 5. Nondimensional length scales as a function of nondimensional time.

shock waves from the shock tube walls), thus moving the vortex core towards the centerline.

The width, which increased during the compression region, decreases and reaches a second plateau at $L_w \approx 1.25$. The height, however, continues to increase within $2.8 < \tau < 6$ and then decreases in $6 < \tau < 6.9$. The reason for the measured decrease of the height is the suction of the tail of the vortex inside the vortex ring. The tail swirl inside the vortex ring leads to entrainment of the surrounding nitrogen gas into the vortex ring. Later in time, this leads to the splitting of the vortex rings and then the experiment enters the phase of the highly turbulent mixing. During this time the width begins to increase at a constant rate and further tests are needed at longer times to determine if this growth continues or asymptotes to a constant value. Also in this region the L_h and L_v curves appear to begin a constant growth.

The results presented in this Letter describe the development of a shocked spherical density inhomogeneity at a Mach number of 2.88. Previously, shock tubes have only studied these instability growth rates at lower Mach numbers (< 1.5) and it is of interest to connect the hydrodynamic shock instability growth measurements with those conducted in laser driven shock tubes at higher Mach numbers (> 10). It is thought that at Mach numbers where the particle velocity behind the incident shock wave becomes supersonic (for a shock in nitrogen at atmospheric temperature this occurs at $M = 2.07$), there are compressibility effects that may alter the growth of the bubble. The above data present high quality images of shocked bubbles in the regime where the particle velocity behind the shock is supersonic and give detailed measurements of the growth rates for several parameters of the shocked bubble evolution. Several features were identified and described including the presence of a secondary vortex ring, which was predicted previously for strong shocks, but until now, not confirmed experimentally.

This research was sponsored by the National Nuclear Security Administration under the Stewardship Science Academic Alliances program through DOE Research Grant No. DE-FG52-03NA00061.

---

*Electronic address: bonazza@engr.wisc.edu
Electronic address: http://silver.neep.wisc.edu/~shock/

[1] R. D. Richtmyer, Commun. Pure Appl. Math. **13**, 297 (1960).
[2] Y. Y. Meshkov, NASA Tech. Transl. **F-13**, 074 (1970).
[3] G. Rudinger and L. M. Somers, J. Fluid Mech. **7**, 161 (1960).
[4] J.-F. Haas and B. Sturtevant, J. Fluid Mech. **181**, 41 (1987).
[5] J. M. Picone and J. P. Boris, J. Fluid Mech. **189**, 23 (1988).
[6] N. Cowperthwaite, Physica (Amsterdam) **37D**, 264 (1989).
[7] J. W. Jacobs, Phys. Fluids A **5**, 2239 (1993).
[8] S. Zhang, N. J. Zabusky, G. Peng, and S. Gupta, Phys. Fluids **16**, 1203 (2004).
[9] H. F. Robey, T. S. Perry, R. I. Klein, J. O. Kane, J. A. Greenough, and T. R. Boehly, Phys. Rev. Lett. **89**, 085001 (2002).
[10] R. I. Klein, K. S. Budil, T. S. Perry, and D. R. Bach, Astrophys. J. **583**, 245 (2003).
[11] M. H. Anderson, B. P. Puranik, J.. Oakley, P. W. Brooks, and R. Bonazza, Shock Waves **10**, 377 (2000).
[12] P. B. Puranik, J. G. Oakley, M. H. Anderson, and R. Bonazza, Shock Waves **13**, 413 (2004).
[13] K. Mysels, K. Shinoda, and S. Frankel, *Soap Films* (Pergamon, New York, 1959).
[14] C. Isenberg, *The Science of Soap Films and Bubbles* (Tieto Ltd., England, 1978).
[15] A. L. Yarin, *Free Liquid Jets and Films: Hydrodynamics and Rheology* (Longman Science and Technology and John Wiley and Sons, New York, 1993).
[16] R. D. Cohen, Proc. R. Soc. A **435**, 438 (1991).
[17] N. J. Zabusky and S. M. Zeng, J. Fluid Mech. **362**, 327 (1998).
[18] G. Layes, G. Jourdan, and L. Houas, Phys. Rev. Lett. **91**, 174502 (2003).
[19] J. J. Quirk and S. Karni, J. Fluid Mech. **318**, 129 (1996).